INFRARED SPECKLE IMAGING: DATA REDUCTION WITH APPLICATION TO BINARY STARS

J.C. CHRISTOU
Kitt Peak National Observatory
*National Optical Astronomy Observatories**
P.O. Box 26732, Tucson, AZ 85726-6732, U.S.A.

(Received 18 January, 1991; accepted 13 March, 1991)

Abstract. The extended Knox-Thompson reduction scheme currently in use at Kitt Peak National Observatory and Steward Observatory for the reduction of infrared speckle interferometry is described in detail. Applications of this algorithm and the less computationally intensive shift-and-add analysis to both simulated and real binary star data is presented demonstrating that the latter may be successfully used for image reconstruction by using a separately measured point source. The performance of both techniques is shown to improve by application of an iterative deconvolution algorithm to apply *a priori* image constraints without degradation of photometric information.

Key words: Infrared Speckle Imaging - Shift-and-add - Binary Stars - Knox-Thompson - High Spatial Resolution

1. Introduction

With the availability of two-dimensional infrared array detectors, infrared speckle interferometry and imaging are now fully possible. Two such cameras have already been built and are now being routinely used at Kitt Peak National Observatory (KPNO) (Beckers *et al.*, 1988) and Steward Observatory (SO) (McCarthy *et al.*, 1990) and others are being developed. The two existing systems utilise the Santa Barbara Research Corporation 58 × 62 InSb detector and are designed to Nyquist sample the images at or beyond the full diffraction-limit of the KPNO Mayall 4m (effective aperture = 3.76m) for the KPNO system and both the SO 2.3m as well as the cophased Multiple Mirror Telescope (MMT) (effective aperture = 6.86m) for the SO system.

Now that scientific results are being produced from these cameras (Christou *et al.*, 1991; Zinnecker *et al.*, 1991; McCarthy *et al.*, 1991a; Dougados *et al.*, 1991a,b) it is appropriate to summarize the data reduction procedures currently being employed by both systems. The scientific programs include the investigation of circumstellar regions for extended emission and scattering but the majority are surveys for multiplicity especially among pre-main sequence objects and nearby low-mass stars. Although a number of such objects has been investigated with one-dimensional slit-scanning techniques, the benefits of two-dimensional studies are that all position angles are simultaneously investigated and that tertiary systems are far less ambiguously

* Operated by the Association of Universities for Research in Astronomy Inc. (AURA) under cooperative agreement with the National Science Foundation

Experimental Astronomy **2**: 27–56, 1991.

detected. The incidence of multiplicity among both groups is basically unknown and direct measurements of the companion masses and colours are important to the general understanding of both the mass-luminosity relation for the low-mass region of the main sequence and the conditions of stellar formation. Thus detection of companions is not sufficient. Reliable measurements of not only their separations but also their magnitude differences, and therefore their colours, are essential.

The primary data reduction algorithm used is a modified version of the fully rigourous extended Knox-Thompson cross-spectrum analysis (Knox, 1976) which is generally applicable to all objects. It is described in detail in the following section. Recently, aperture synthesis techniques have also been applied to data obtained with these cameras and the results compare well with those obtained from the cross-spectrum analysis (Haniff *et al.*, 1990).

The more heuristic simple shift-and-add (SAA) analysis (Bates & Cady, 1980) has also been employed for point source dominated objects. The SAA analysis shifts each short exposure image or specklegram on its brightest speckle and then stacks on it. This results in improved resolution and Strehl ratio (McCarthy *et al.*; 1991b, Christou, 1991). The resulting SAA image consists of a diffraction-limited core sitting atop a diffuse seeing background. This technique works well for high-contrast objects where there is a bright point or point-like source. However, it breaks down for a broad extended object, i.e. low-contrast, as there is then no bright speckle to lock onto. It has been found to be a useful diagnostic tool for determining whether an object is resolved. However its ability to be used as an accurate amplitude preserving imaging tool when applied to binary star data has not been thoroughly investigated, especially its ability to be accurately calibrated by a point source measurement. A more thorough discussion of the technique and its variations is given by Hege (1988) and references therein.

This paper outlines the data reduction procedures employed for infrared speckle imaging. It also investigates the capability of the SAA analysis to provide images equivalent to the more rigourous cross-spectrum analysis. In addition binary star photometry and astrometry resulting from both approaches are compared. Scientific interpretation of the results will be presented elsewhere.

2. Data Reduction

2.1. OBSERVING PROCEDURE

A typical observing sequence consists of the following: data frames (specklegrams) of (i) the program object, (ii) a nearby point source reference, and (iii) nearby sky to each. Typically the data is obtained in blocks of 500 specklegrams alternating between the object and the point source reference in an

effort to minimise effects due to differences in the mean atmospheric seeing of each. The frame rate for the KPNO camera is $\sim$ 5 Hz and for the SO camera is $\sim$ 10 Hz. Sky frames are typically taken before and after the data sequence. For background-limited data, i.e. $\lambda \geq 3.4\mu$m, the sky is measured more often because of its variability. Dark current frames, obtained with a closed shutter at the same exposure time, are taken periodically during the night. These are a check of the detector array stability.

2.2. DATA PREPROCESSING

Before data reduction procedures are applied, it is first necessary to "clean" the original data frames. This consists of (a) removing the background from each frame, and correction of (b) flat-field, and (c) both "hot" and "dead" pixels in the array. A mean sky frame, which includes the dark current, is subtracted from each specklegram, including sky data, to place the signal on a zero-mean background. The hot and dead pixels are interpolated over by the mean of the nearest neighbours. For the KPNO detector there is a region of $\sim$ 15 bad pixels centered on pixel (50,10) which is corrected by using a least-squares bi-cubic interpolator from the surrounding good pixels. Pixel-gain calibration (i.e. flat fielding) has proven to be more difficult due to the short exposure times. For the non-thermal data presented herein, the sky exposures do not have sufficient signal for flat field calibration. Experiments with dome-flats measurements and long-exposure sky frames can degrade the computed spectra. For the data presented here no flat-field was used.

2.3. DATA PROCESSING

Each specklegram, excluding sky data, is centroided on its center-of-mass and then apodised by a 10 pixel wide rectangular cosine bell window which takes the frame boundaries to zero thus avoiding the sharp cut-off of the detector field. It is then placed in a 128 $\times$ 128 array to prevent aliasing. The Fourier transform of each frame is then computed and the appropriate Fourier spectra and their variances are then accumulated (see below). In addition the straight sum of the centroided specklegrams is obtained providing an apodised long exposure image which has been corrected for image motion due to both the atmosphere as well as telescope tracking and guiding errors. Statistics about the frame power, maximum, centroid, and seeing estimates are recorded.

2.4. EXTENDED CROSS-SPECTRUM ANALYSIS

In order to reconstruct an image, both Fourier amplitudes and phases are required. The former are straightforwardly obtained from power spectrum

analysis (Labeyrie, 1970). However a more complicated scheme is necessary to extract the Fourier phases. A version of the Knox-Thompson cross-spectrum procedure (Christou *et al.*, 1988) has been implemented to do this.

Each specklegram can be considered to be the convolution of the object distribution $o(x,y)$ with an instantaneous combined telescope/atmosphere point spread function $p_i(x,y)$ contaminated by additive noise due to electronic noise of the detector and sky emission $n_i(x,y)$ i.e.

$$i_i(x,y) = \{o(x,y) * p_i(x,y)\} + n_i(x,y) \tag{1}$$

where $*$ denotes convolution. If each specklegram has a Fourier transform, $I(u,v)$, then the ensemble average cross-spectrum can be written as

$$\mathrm{XS}^{\mathrm{I}}(u,v,\Delta u,\Delta v) = \langle I^*(u,v) I(u+\Delta u, v+\Delta v)\rangle \tag{2}$$

where $\langle\cdots\rangle$ indicates the ensemble average and * represents the complex conjugate. Δu and Δv are orthogonal shifts in the Fourier domain. For $\Delta u = \Delta v = 0$ then (2) reduces to the power spectrum $\mathrm{PS}^{\mathrm{I}}(u,v) = \mathrm{XS}^{\mathrm{I}}(u,v,0,0) = \langle |I(u,v)|^2\rangle$. A shift of one pixel in the frequency domain, i.e. $\Delta u = \Delta v = 1$, gives the pair of subplanes $\mathrm{XS}^{\mathrm{I}}(u,v,1,0)$ and $\mathrm{XS}^{\mathrm{I}}(u,v,0,1)$. Note that the spatial frequency sampling is $\Delta f = 1/(128\Delta r)$ where $\Delta r = \Delta x = \Delta y$ is the image plane sampling. Five orthogonal sub-plane pairs are generally computed (see section 5.3).

The cross-spectrum of the program object (2) can be rewritten as

$$\begin{aligned}\mathrm{XS}^{\mathrm{I}}(u,v,\Delta u,\Delta v) \;=\; & \{O^*(u,v)\cdot O(u+\Delta u, v+\Delta v)\cdot \\ & \cdot\langle P^*(u,v)\cdot P(u+\Delta u, v+\Delta v)\rangle\} + \\ & +\langle N^*(u,v)\cdot N(u+\Delta u, v+\Delta v)\rangle + \\ & + \text{cross} - \text{terms}\end{aligned} \tag{3}$$

which can be rewritten as

$$\begin{aligned}\mathrm{XS}^{\mathrm{I}}(u,v,\Delta u,\Delta v) \;=\; & \left\{\mathrm{XS}^{\mathrm{O}}(u,v,\Delta u,\Delta v)\cdot \mathrm{XS}^{\mathrm{P}}(u,v,\Delta u,\Delta v)\right\} + \\ & + \mathcal{N}^{\mathrm{I}}(u,v)\end{aligned} \tag{4}$$

where $\mathrm{XS}^{\mathrm{O}}(u,v,\Delta u,\Delta v)$ is the object cross-spectrum, $\mathrm{XS}^{\mathrm{P}}(u,v,\Delta u,\Delta v)$, the ensemble average telescope/atmosphere cross-spectrum, i.e. the transfer function for the process, and $\mathcal{N}_I(u,v)$ the additive noise terms. The cross-spectrum transfer function can be estimated from the measurements of the point source reference. At infrared wavelengths typical values of the ratio of the aperture diameter to the atmospheric coherence length D/r_0 values are small (≤ 10). Fluctuations of r_0, due to either airmass or temporal effects, can introduce "seeing effects" such that the transfer fuction estimated from the point source is not equivalent to that for the program object. Errors

due to these seeing effects have been discussed previously (Christou *et al.*, 1987b; Perrier & Mariotti, 1987) and binning schemes for their correction are reviewed by Perrier (1989) and Haas (1990).

However, both object and point source cross-spectra need to be corrected for the additive noise terms before the transfer function calibration (Christou, 1988). The sky data cross-spectrum, i.e. the third term in (3), is the dominant noise term except at low signal-to-noise levels per speckle-gram where the cross-terms become important. In general $\mathcal{N}^{\mathrm{I}}(u,v) \sim \langle N^*(u,v) \cdot N(u+\Delta u, v+\Delta v)\rangle$. The noise corrected object cross-spectrum is then calibrated for the combined telescope/atmosphere transfer function by dividing by the noise corrected point source cross-spectrum. For the results presented here, no attempt at binning the data according to r_0 was attempted due to the relatively small number of frames. However, depending upon the stability of the seeing conditions, the individual data blocks were reduced separately or *en masse*.

An initial estimate for the object Fourier modulus is then simply obtained by square rooting the seeing corrected power spectrum, i.e.

$$E[|O(u,v)|] = \sqrt{\mathrm{XS}^{\mathrm{O}}(u,v,0,0)} = \left[\frac{\mathrm{XS}^{\mathrm{I}}(u,v,0,0) - \mathcal{N}^{\mathrm{I}}(u,v,0,0)}{\mathrm{XS}^{\mathrm{P}}(u,v,0,0) - \mathcal{N}^{\mathrm{P}}(u,v,0,0)}\right]^{\frac{1}{2}} \quad (5)$$

for $(u,v) \leq D/\lambda$.

The Fourier phases are more difficult to extract. The phases contained in the final corrected cross-spectrum, $\mathrm{XS}^{\mathrm{O}}(u,v,\Delta u,\Delta v)$, are the phase differences $\theta(u,v)$ of the true object phases $\phi(u,v)$, i.e.

$$\mathrm{XS}^{\mathrm{O}}(u,v,\Delta u,\Delta v) = O^*(u,v)O(u+\Delta u, v+\Delta v) \quad (6)$$

such that

$$\begin{aligned} \arg\{\mathrm{XS}^{\mathrm{O}}(u,v,\Delta u,\Delta v)\} &= \theta(u,v,\Delta u,\Delta v) \\ &= -\phi(u,v) + \phi(u+\Delta u, v+\Delta v) \end{aligned} \quad (7)$$

where the complex object spectrum can be expressed as $O(u,v) = |O(u,v)| \exp[i\phi(u,v)]$.

In order to extract the phases from the multiple phase differences contained in the cross-spectrum a complex phasor recursion is used which retrieves the full complex spectrum, i.e.

$$E[O(u+\Delta u, v+\Delta v)] = \frac{\mathrm{XS}^{\mathrm{O}}(u,v,\Delta u,\Delta v)}{E[O^*(u,v)]} \quad (8)$$

The recursion is initialised by setting $E[O(0,0)] = |O(0,0)|$, because the spectrum for a real object is real-valued at zero spatial frequency, and the higher spatial frequency components are computed by integrating outward

from the origin. The cross-spectra are accumulated for the entire (u, v) domain which allows the complex object spectrum to be recovered from each quadrant independently. The two half planes are then averaged together using Hermitian constraints.

The recursive procedure is outlined as follows. Considering the $u > 0, v > 0$ quadrant then

$$E[O(u,v)] = \sum_{\Delta u, \Delta v}^{M} \left[w_{\Delta u}(u,v) \left(\frac{\mathrm{XS}^{\mathrm{O}}(u - \Delta u, v, \Delta u, 0)}{O^*(u - \Delta u, v)} \right) + w_{\Delta v}(u,v) \left(\frac{\mathrm{XS}^{\mathrm{O}}(u, v - \Delta v, 0, \Delta v)}{O^*(u, v - \Delta v)} \right) \right] \cdot \left[\sum_{\Delta u, \Delta v}^{M} [w_{\Delta u}(u,v) + w_{\Delta v}(u,v)] \right]^{-1} \tag{9}$$

for $\Delta u, \Delta v > 0$. M is the number of orthogonal subplanes used and $w_{\Delta u}(u,v)$ and $w_{\Delta v}(u,v)$ are variance weights, i.e. inverse of the variances, of each quotient. The variances at each stage of the reduction process, e.g. noise calibration, point-source calibration etc., are computed by standard error propagation (Bevington, 1969) using a Taylor series approximation neglecting both higher-order and cross-terms.

This integration scheme accumulates large errors at the high spatial frequencies. These errors can be distributed in the (u, v) domain by applying least squares techniques to minimise the differences between the measured phase differences and those contained in the initial estimate $E[O(u,v)]$. An iterative scheme suggested by von der Lühe (1987) based upon the successive over-relaxation scheme (SOR) described by Southwell (1980) is used. i.e.

$$O_{k+1}(u,v) = O_k(u,v) + \omega \{ \mathrm{d}O_k(u,v) - O_k(u,v) \} \tag{10}$$

where ω is the SOR relaxation parameter and $\mathrm{d}O_k(u,v)$ is the variance-weighted average of the complex vector at (u,v) obtained from the four neighbouring spatial frequency locations, i.e. $(\Delta u, 0)$, $(0, \Delta v)$, $(-\Delta u, 0)$, and $(0, -\Delta v)$, for each orthogonal pair of sub-planes. The optimal value for ω is given by Southwell (1980) as

$$\omega = \frac{2}{1 + \sin[\pi/(N+1)]} \tag{11}$$

where N is the side of the array so that $\omega = 1.95$ (for $N = 128$). A spiral path is followed, working out from the higher-SNR low spatial frequencies to the lower-SNR high spatial frequencies. This path continually updates the complex spectrum and alternates direction with successive iterations.

The convergence of the fit is followed from either the RMS phase difference residuals or the RMS phase iteration differences contained within the aperture cut-off frequency, i.e. $(u,v) \leq D/\lambda$. Typically convergence occurs within 30–50 iterations. A comparison of SOR with a similar scheme, which is a variant of the Hudgin algorithm (Ebstein, 1987), shows the former to have faster convergence (Christou *et al.*, 1988). A similar integration and relaxation scheme is sucessfully used by the Harvard/CfA group (Nisenson, 1989) for the reduction of visible photon-limited speckle data.

2.5. SHIFT-AND-ADD ANALYSIS

By comparison the SAA analysis is much simpler. The mean SAA image is accumulated by stacking the specklegrams on the brightest speckle in each, i.e.

$$s(x,y) = \frac{1}{K}\sum_{k=1}^{K} i_k(x+x_k, y+y_k) \tag{12}$$

where (x_k, y_k) represents the location of the brightest speckle in the k^{th} specklegram and K is the total number of specklegrams. Using the formalism of (1), this expression can be rewritten as

$$s(x,y) = [o(x,y) * p_s(x,y)] + n_o(x,y) \tag{13}$$

where $p_s(x,y)$ is an object dependent point spread function consisting of a background fog and a diffraction-limited core (Bates, 1982; Bates & Davey, 1987). For point-source dominated objects, the point spread function can be estimated from SAA analysis of an unresolved star. The object SAA image was calibrated by the equivalent point source SAA image, i.e. $s_*(x,y) = p_s(x,y) + n_p(x,y)$. Both SAA images are accumulated after the preprocessing discussed above. Due to the random shifting in the image domain, as well as the random nature of the read noise and sky emission, the noise term in the final SAA image can be considered as random and zero-mean.

Generally, one of the major advantages of SAA imaging is its simplicity. No Fourier transforms are usually required. However, for the iterative deconvolution analysis, discussed below, the errors of the Fourier components are required. Thus it is necessary to accumulate the raw shift-and-add image in the Fourier domain, i.e.

$$S(u,v) = \frac{1}{K}\sum_{k=1}^{K} I_k(u,v)\exp[-i(x_k u + y_k v)] \tag{14}$$

where $I_k(u,v)\exp[-i(x_k u + y_k v)]$ is the Fourier transform of the peak translated specklegram $i_k(x+x_k, y+y_k)$ so that $S(u,v) = \mathrm{FT}[s(x,y)]$ due to

the distributive nature of the Fourier integral. It has been found that the random noise terms can be approximated as "white" noise which can be removed by measuring the mean value for spatial frequencies $(u, v) > D/\lambda$ and subtracting.

3. Iterative Deconvolution

Post-processing algorithms are typically applied to "clean up" the images after the basic processing steps described above. There are a number of algorithms available which show some degree of success. These algorithms allow *a priori* image constraints to be applied to the reconstructed images, such as non-negativity and object support. Due to the inherent non-linearity of such algorithms it is important to constrain them to the statistical uncertainties in the measured quantities. A technique which permits this is the iterative deconvolution approach suggested by Ayers (1989). This algorithm was initially applied to one-dimensional cross-spectrum analysis on infrared speckle data but it is readily extendable to two dimensions (Christou, 1990) and for a variety of data reduction schemes. It is a more generally applicable technique for applying *a priori* constraints than the iterative transform algorithm (reviewed by Dainty & Fienup, 1987) in that the full object complex visibility is allowed to vary, not only the Fourier phases. Furthermore the variation is constrained by the errors in the measured spectra.

The algorithm has not only been applied to the two-dimensional extended Knox-Thompson analysis described above but also to deconvolution of shift-and-add images. The advantage of this technique is that even though the constraints are applied in the image domain, the corresponding Fourier spectrum is only allowed to vary within a 3σ volume determined by its measurement error. This produces the best constraint-limited image to the measured Fourier components and permits amplitude ratios to be preserved unlike various other techniques, most notably some implementations of maximum entropy (Skilling & Bryan, 1984). Note that to apply this technique, the statistical errors of all the measured quantities are required and must be accumulated along with their means.

3.1. CROSS-SPECTRUM APPLICATION

For cross-spectrum analysis the iterative deconvolution procedure is outlined as follows. Note that all errors are recomputed along with the updated values by propagating the standard errors of the measured quantities through all the analysis.

1. An initial object estimate $E[o(x, y)]$ is obtained by inverting the Fourier modulus and phases obtained with the power spectrum/cross-spectrum analysis described above. In order to ensure that the point spread function is

positive and that only measured spatial frequencies are used, the Fourier transform of an Airy beam $A(u,v)$ is used to apodise the Fourier amplitudes, i.e.

$$E[o(x,y)] = \mathrm{FT}^{-1}[E[|O(u,v)|\exp[i\phi(u,v)]] \cdot A(u,v)] \tag{15}$$

The size of the beam is not solely determined by the telescope aperture but also by the spatial frequency where the additive sky and detector noise becomes dominant. This therefore depends upon the object brightness and at longer wavelengths on the thermal sky emission. Even though the final images are produced with a Gaussian beam (see §4), an Airy beam is used as this has an upper spatial frequency limit above which no information is transmitted. A Gaussian beam transmits at all spatial frequencies so that strong high-spatial frequency noise, beyond the effective cut-off frequency, may affect the negativity in the image.

2. *A priori* image constraints are applied, e.g. non-negativity $o_i(x,y) = \mathrm{POS}[E[o(x,y)]]$ where $\mathrm{POS}[\cdots]$ has the effect

$$o_i(x,y) = E[o(x,y)] \text{ for } E[o(x,y)] > 0$$
$$o_i(x,y) = 0 \text{ for } E[o(x,y)] \leq 0$$

and the i subscript refers to the i^{th} iteration.

3. The non-negative image is Fourier transformed and the Fourier transform of the Airy beam is divided out, i.e.

$$O_i(u,v) = \frac{\mathrm{FT}[o_i(x,y)]}{A(u,v)} = |O_i(u,v)|\exp[i\phi_i(u,v)]$$

to obtain new modulus and phase estimates.

4. A new power spectrum is computed, i.e. $\mathrm{PS}_i^{\mathrm{O}}(u,v) = |O_i(u,v)|^2$. This is compared with the initial power spectrum estimate $\mathrm{PS}^{\mathrm{O}}(u,v)$, i.e. if

$$|\mathrm{PS}_i^{\mathrm{O}}(u,v) - \mathrm{PS}^{\mathrm{O}}(u,v)| > 3\sigma_{\mathrm{PS}}(u,v)$$

where $\sigma_{\mathrm{PS}}(u,v)$ are the measured power spectrum mean errors, then

$$|O_i'(u,v)| = |O_{\mathrm{est}}(u,v)|$$

otherwise

$$|O_i'(u,v)| = |O_i(u,v)|$$

where the $'$ indicates modulus update after power spectrum comparison.

5. An updated Fourier spectrum is computed using this improved modulus, i.e.

$$O_i'(u,v) = |O_i'(u,v)|\exp[i\phi_i(u,v)]$$

which gives the updated cross-spectrum i.e.

$$\mathrm{XS}_i^{\mathrm{O}}(u,v,\Delta u,\Delta v) = O_i^{*\prime}(u,v)\cdot O_i^{\prime}(u+\Delta u, v+\Delta v)$$

6. This is compared with initial cross-spectrum estimate $\mathrm{XS}^{\mathrm{O}}(u,v,\Delta u,\Delta v)$, such that if

$$|\mathrm{XS}_i^{\mathrm{O}}(u,v,\Delta u,\Delta v) - \mathrm{XS}^{\mathrm{O}}(u,v,\Delta u,\Delta v)| > 3\sigma_{\mathrm{XS}}(u,v,\Delta u,\Delta v)$$

where $\sigma_{\mathrm{XS}}(u,v)$ are the measured cross-spectrum mean errors, then new estimates of the object spectrum are computed from the measured cross-spectrum, i.e.

$$O_i''(u,v) = \frac{\mathrm{XS}^{\mathrm{O}}(u-\Delta u, v-\Delta v, \Delta u, \Delta v)}{O_i^{*\prime\prime}(u-\Delta u, v-\Delta v)}$$

otherwise

$$O_i''(u,v) = O_i'(u,v)$$

where the $''$ indicates complex visibility update after cross-spectrum comparison.

7. The new image estimate $o_i''(x,y)$ for the i^{th} iteration is computed from the updated Fourier spectrum.

8. Repeat steps 2–7 with $E[o(x,y)] = o_i''(x,y)$.

The performance of the algorithm can be monitored by following the percentage negative power at each iteration and convergence is determined from a χ^2 error metric, i.e.

$$\chi^2 = \sum_{u,v}\left|\frac{\mathrm{PS}^{\mathrm{O}}(u,v) - \mathrm{PS}_i^{\mathrm{O}}(u,v)}{\sigma_{\mathrm{PS}}(u,v)}\right|^2 + \sum_{u,v,\Delta u,\Delta v}\left|\frac{\mathrm{XS}^{\mathrm{O}}(u,v,\Delta u,\Delta) - \mathrm{XS}_i^{\mathrm{O}}(u,v,\Delta u,\Delta v)}{\sigma_{\mathrm{KT}}(u,v,\Delta u,\Delta v)}\right|^2 \tag{16}$$

where the summations are over the aperture sampled spatial frequencies and all cross-spectrum planes. Typically $\sim 20 - 30$ iterations are required.

3.2. SHIFT-AND-ADD APPLICATION

The iterative deconvolution of SAA images is simpler to apply than for the cross-spectrum application. The measured quantities are the Fourier transforms of the SSA images and the process is constrained by their measured errors.

1. The "raw" shift-and-add images and their corresponding Fourier domain errors of both the object $s(x,y)$ and the point source reference $s_*(x,y)$ are

generated as described above. An initial object estimate $E[o(x,y)]$ is obtained by performing a simple deconvolution with an appropriate Airy filter, i.e.

$$E[o(x,y)] = \mathrm{FT}^{-1}\left[\frac{\mathrm{FT}[s(x,y)]}{\mathrm{FT}[s_*(x,y)]} \cdot A(u,v)\right] = \mathrm{FT}^{-1}[O_s(u,v) \cdot A(u,v)]$$

2. Firstly the non-negativity constraints are applied, i.e. $o_i(x,y) = \mathrm{POS}[E[o(x,y)]]$.

3. The Fourier transform of the non-negative image is computed and the Airy beam is removed, i.e.

$$O_i(u,v) = \frac{\mathrm{FT}[o_i(x,y)]}{A(u,v)} = |O_i(u,v)| \exp[i\phi_i(u,v)]$$

4. This is compared to the original spectrum i.e.

If $|O_i(u,v) - O_s(u,v)| > 3\sigma_s(u,v)$

where $\sigma_s(u,v)$ are the mean errors on $|O_s(u,v)|$, then

$$O_i'(u,v) = O_s(u,v)$$

otherwise

$$O_i'(u,v) = O_i(u,v)$$

Note that the complex visibility, i.e. modulus and phases, is adjusted.

5. The updated complex visibility is apodised and Fourier inverted to produce a new image $o_i'(u,v)$.

6. Steps 2–5 are repeated with $E(o(x,y)] = o_i'(x,y)$.

The procedure can be monitored by following the percentage of negative power in the resulting image at each iteration and convergence determined from a normalised root-mean-square error metric (NRMS) which can be expressed as

$$\mathrm{NRMS} = \left[\frac{\sum_{u,v}[|O_i(u,v) - O_{\mathrm{SAA}}(u,v)|]^2}{\sum_{u,v}|O_{\mathrm{SAA}}(u,v)|^2}\right]^{\frac{1}{2}} \tag{17}$$

where the summation is over the spatial frequencies sampled by the aperture.

4. Application To Simulated Data

In order to both test the algorithms and also to investigate their effectiveness, simulated data were used as the "true" object is known. The simulations were computed using an algorithm previously described (Christou *et al.*, 1987a). The model assumed a 3.8 metre pupil with 1″ seeing at 500 nm

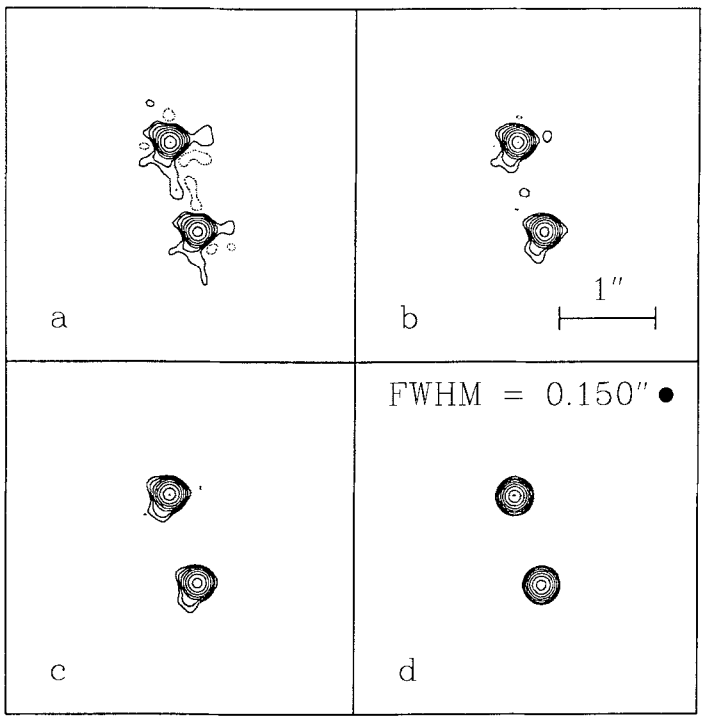

Fig. 1. Reconstructed images for the first simulated binary (a) before and (b) after the phase relaxation, (c) after iterative deconvolution compared to (d) the true object. Contour levels at -4, -2, -1% (dotted lines) and 1, 2, 4, 8, 16, 32, 64, & 99% (solid lines). (Note that all contour plots use the same levels.) For all the images N is up and E is left.

(corresponding to an r_0 of 60 cm at the simulated observing wavelength of 2.2 μm). Two binary stars were chosen as the test objects, the first had a flux ratio of 0.85 and was well resolved with a separation of 0.″939 compared to the telescope resolution of $\lambda/D = 0.''120$. The second had a much fainter secondary, flux ratio of 0.10, at a separation of 0.″202. Two statistically independant data sets were generated for each object. One for the binary and one as the point source reference. Each consisted of 500 simulated specklegrams. Note that a typical data set contains at least $\sim$ 1500-2500 specklegrams. All specklegrams were "contaminated" by additive zero-mean Gaussian noise to simulate the random readout noise of the system. Systematic detector noise was not simulated. This signal-to-noise simulates a K magnitude of 5.6 for both objects assuming no signal loss due to internal reflections of the telescope and detector for a narrow band K filter with 50 ms exposures.

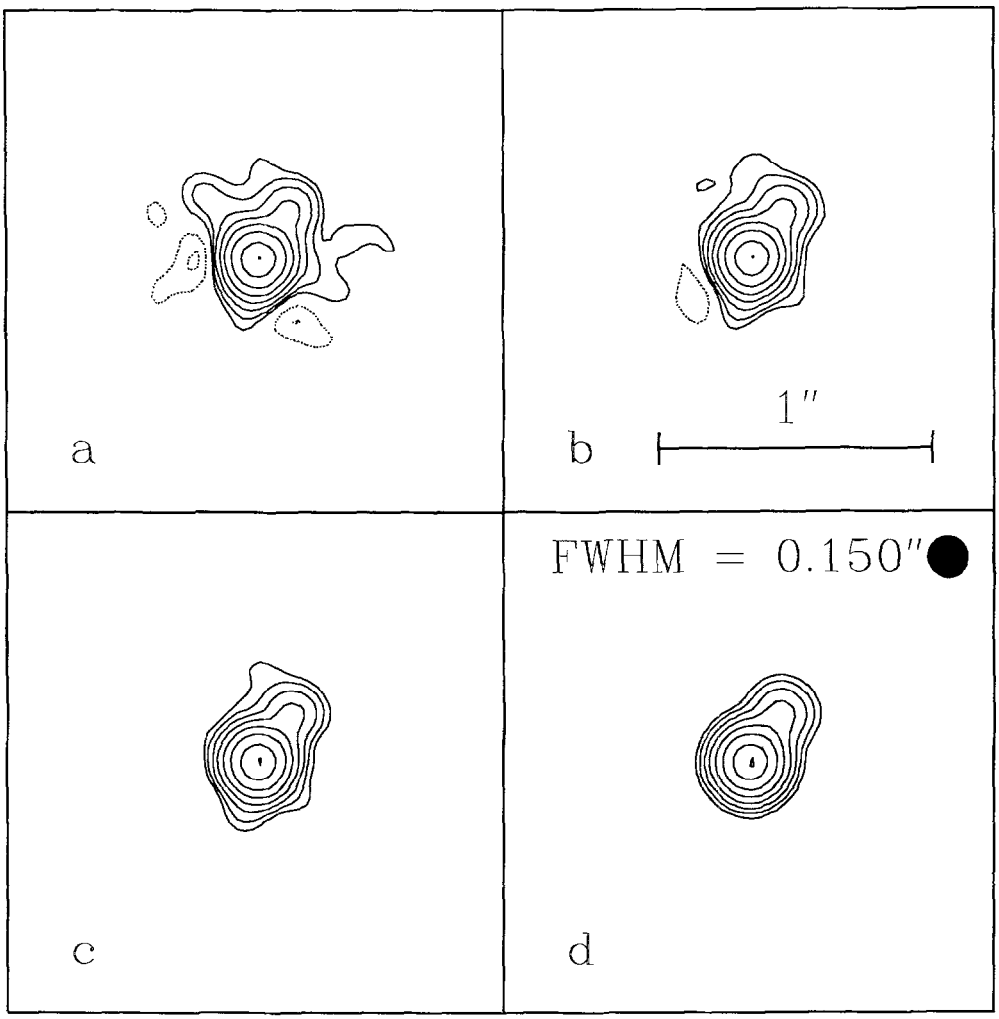

Fig. 2. As figure 1 but for the second simulated binary.

4.1. CROSS-SPECTRUM IMAGES

Figures 1 & 2 show contour plots for image reconstructions of the two simulated binaries respectively compared to the "true" objects. All were restored with a Gaussian beam of FWHM 0.″150. This beam size is larger than the 0.″120 diffraction-limit because of the additive noise. The logarithmic contour levels are chosen to emphasize the low intensities of the reconstructions. Because the data is well behaved due to its simulated nature, there is little difference between the images from the two phase estimates, however an

TABLE I
Binary star parameters from fitting simulated data (XS)

Object		Intensity Ratio	Separation (″)	Position Angle (°)
Binary 1	True	0.850	0.939	253
	Image	0.838	0.939	253
	Modulus	0.837	0.939	253
Binary 2	True	0.100	0.202	124
	Image	0.091	0.209	124
	Modulus	0.100	0.202	124

improvement is seen. There is also very little negative power in the images so that the iterative deconvolution has a small effect. Visual inspection of the images shows that the amplitude ratio has been preserved at all stages.

The Fourier components, rather than the images, are the direct output of the speckle analysis. Figure 3 shows these Fourier components for the second binary. The true object modulus and phase are shown in (a) and (b) respectively; the power spectrum moduli and relaxed phases in (c) and (d) respectively and the modulus and phases after the iterative deconvolution in (e) and (f) respectively. Note the "noisy" structure of the recovered modulus and phases due to the low number of simulated specklegrams and also note the neighbourhood averaging after the iterative deconvolution.

4.1.1. Binary Star Parameters.

Determination of the binary star parameters can quantitatively test how good the object reconstruction is. These parameters can be obtained either from the image or the Fourier domains. To do this an iterative non-linear least-squares algorithm was employed to obtain the x & y locations of each component as well as the intensity ratio. For the image domain the model comprised two Gaussians of FWHM equal to that used for image reconstruction. For the Fourier domain, only the reconstructed modulus was fit by a model representing the Fourier modulus of two point sources. Table I summarizes the results obtained for the two simulated binaries.

For the first binary, the fit parameters agreed well between the two domains. The separation and position angles are accurately determined, however the intensity ratio was $\sim$ 1% too low in both cases, corresponding to a magnitude underestimate of $\sim$ 0.01! For the second object with the fainter companion, the separation was not as well determined from the image fit, being $\sim$ 0.″01 out. However, as the image scale was sampled at only 0.″056/pixel, this is a very good agreement for 3.6 pixel separation. The

intensity ratio from the modulus estimate is excellent and for the image determination is also $\sim$ 1% too low. This is indicative of the 1% – 2% features seen in the image reconstructions in figures 1 and 2.

4.2. SHIFT-AND-ADD IMAGES

Figures 4 & 5 show the deconvolved shift-and-add images for the same two binary stars (a) before and (b) after iterative deconvolution. In figure 4a a "ghost" secondary is clearly seen at the 2% level. Such ghosts are caused by the additive noise occasionally making the brightest speckle in the secondary stronger than that in the primary. In figure 4b this ghost is reduced to $\sim$ 1%. Both data sets show similar low-level structure, $\sim$ 2%, from both reduction procedures which indicates that it is inherent in the data rather than an artifact of either of the processing schemes. For the close binary the shift-and-add result clearly does not recover the secondary at the same intensity as for the cross-spectrum analysis and it is not significantly brighter than the systematics in the reconstruction.

Figure 6 shows the Fourier moduli of the SAA images shown in figure 5 (a) before and (b) after iterative deconvolution. Comparison of 6a with 3c shows the raw SAA moduli to be significantly noisier. Note that similar features are seen in both moduli after applying the iterative deconvolution which are indicative of the systematics seen in the images. Why should the SAA image be noisier? This is straightforward in that the diffraction-limited information is contained in only one speckle, albeit the brightest, whereas for the Fourier analysis *all* speckles are used. Figure 7 shows that the SAA MTF is $\sim$ 1 decade lower at the high spatial frequencies.

4.2.1. Binary Star Parameters.

These parameters were extracted in the same way as for the cross-spectrum results. They are summarized in Table II. As expected from the images the intensity ratios are lower by $\sim$ 3–4% of the peak intensity whereas for the modulus fits they agree very well. This implies that the discrepancy is contained within the SAA Fourier phases. For the second binary the separation and position angles differ from the true values by $\sim$ 5% and $\sim$ 1% respectively. Both modulus and image fitting yield similar values, indicating that these are due to the lower SNR of the SAA process.

4.3. SUMMARY

These simulations demonstrate that both the cross-spectrum analysis and the SAA Fourier modulus analysis yield accuracies to within 0.01 magnitudes which strongly suggests that SAA imaging is an important tool for recovering not only the separation and position angle of binary stars but also their

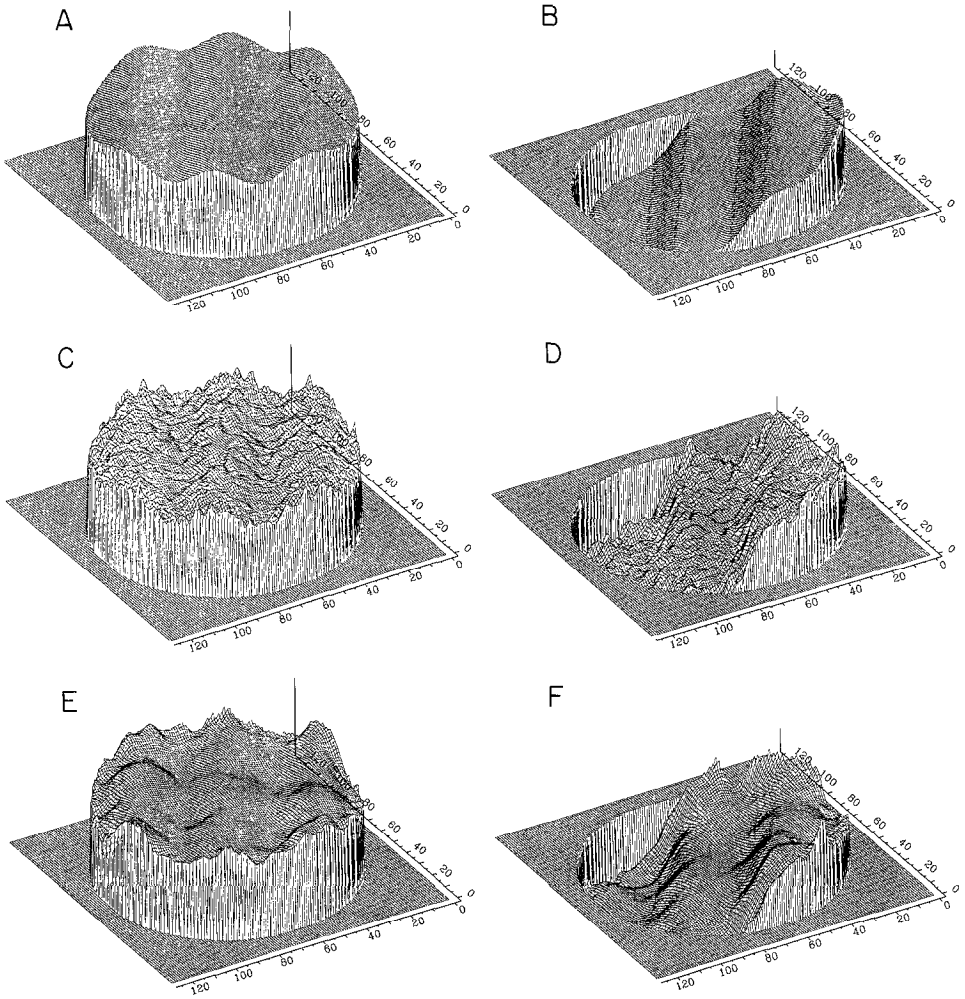

Fig. 3. Fourier components for the second simulated binary. (a) true modulus, (b) true phases, (c) recovered modulus, (d) relaxed phases and (e) modulus and (f) phases after iterative deconvolution.

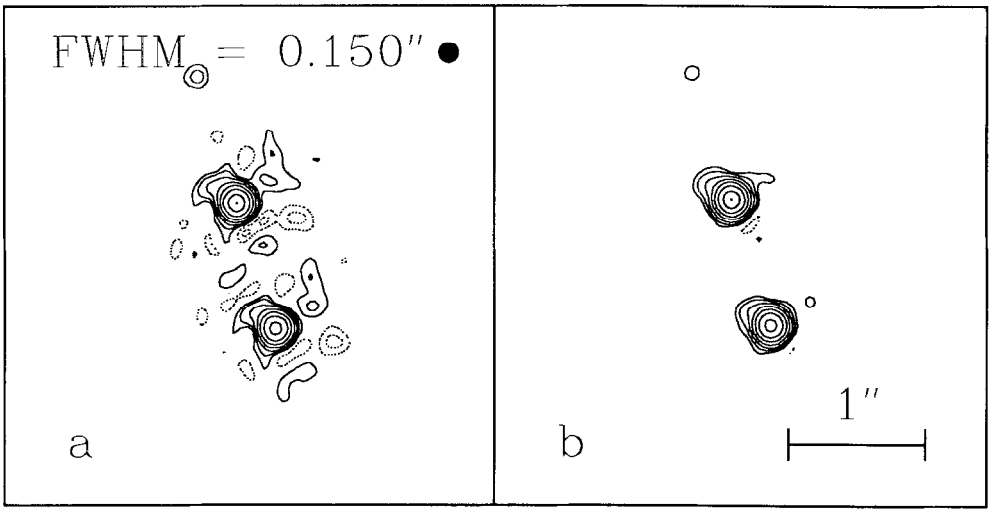

Fig. 4. Deconvolved SAA images for the first simulated binary (a) before and (b) after iterative deconvolution.

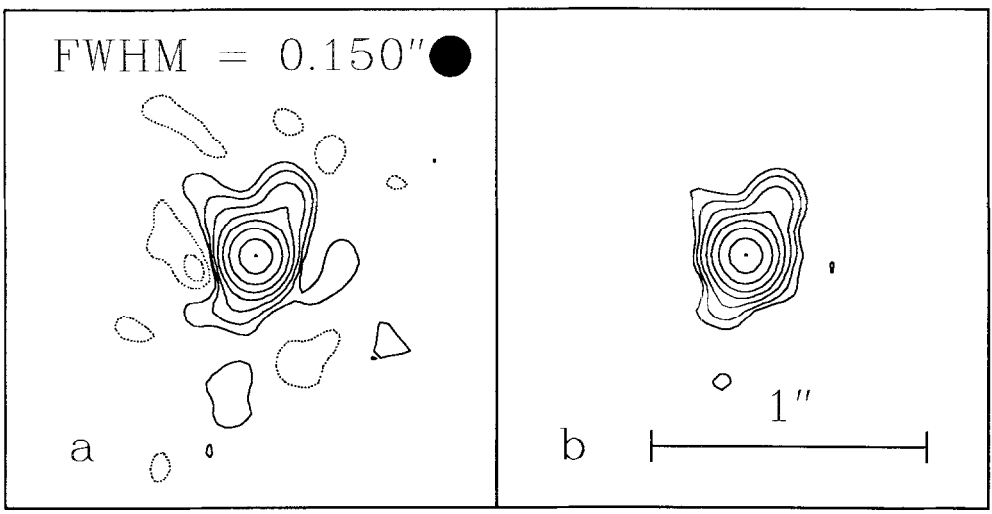

Fig. 5. As figure 4 but for the second simulated binary.

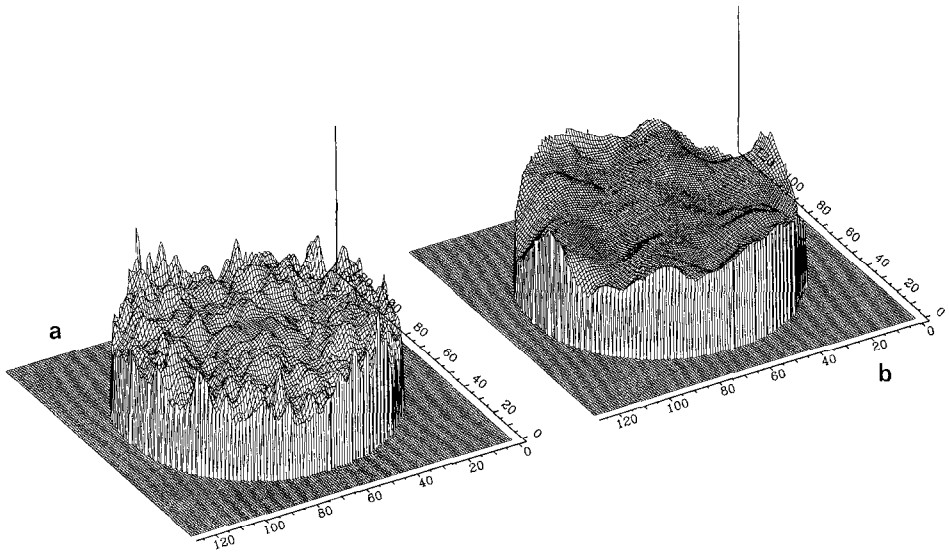

Fig. 6. Fourier moduli of the SAA images of the second simulated binary (a) before and (b) after iterative deconvolution.

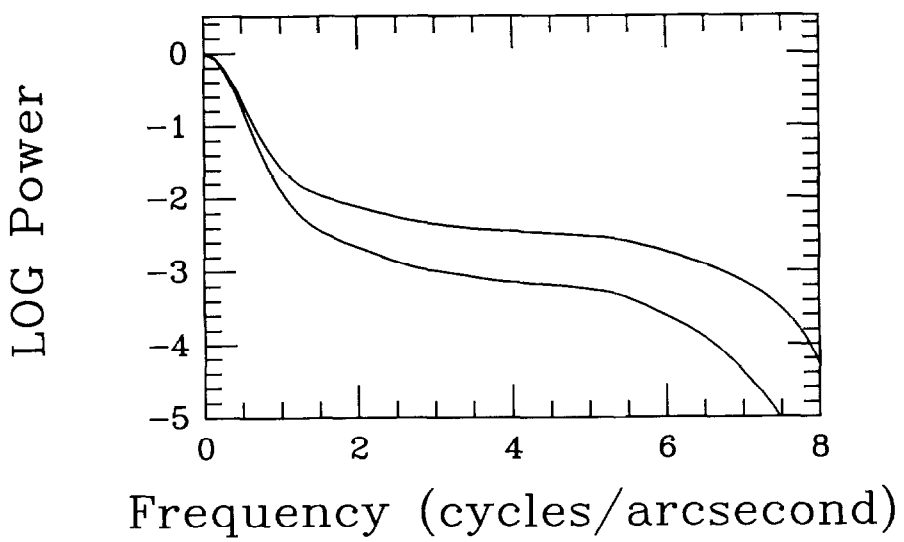

Fig. 7. Comparison of MTF's for power spectrum analysis (top) and SAA (bottom) as measured from simulated point source data. Note that at the higher spatial frequencies there is $\sim$ 1 decade difference favouring the power spectrum analysis.

TABLE II
Binary star parameters from fitting simulated data (SAA)

Object		Intensity Ratio	Separation (″)	Position Angle (°)
Binary 1	True	0.850	0.939	253
	Image	0.813	0.939	253
	Modulus	0.843	0.939	253
Binary 2	True	0.100	0.202	124
	Image	0.064	0.212	121
	Modulus	0.099	0.213	120

TABLE III
Observing parameters

Binary	K	t_{exp} (ms)	λ (μm)	$\Delta\lambda$ (μm)	Seeing FWHM (″)	Air Mass	No. Frames Object	Ref.
1	~ 7	200	2.16	0.38	1.25	2.1	290	170
2	6.5	50	2.16	0.38	0.80	1.1	1493	1952

magnitude differences without the need of the full Fourier analysis. The 180° ambiguity inherent in just fitting the Fourier modulus is nicely resolved from the SAA image. It is interesting to note that images obtained from the SAA analysis show ghosts which remove power from the secondary so that the intensity ratios as measured from the images is smaller. Bagnuolo (1982) has investigated the strengths of these ghosts with simulated data and has found them to persist to the low intensity ratios in the raw SAA images. However, their relative strengths have not been investigated for the deconvolved cases. Investigation of the ghosts in the SAA images indicate that the residual power is indeed located at these positions.

5. Application To Real Data

How well do both techniques work with real data? The two simulated binaries analysed above are typical of survey objects. In this section results are presented for two newly discovered binary stars which have similar characteristics to the two simulations. These objects were observed for two different surveys, one investigating the incidence of multiplicity among low-mass main sequence stars and the other among young pre-main sequence stars. Both sets of observations were taken with the NOAO speckle camera at the KPNO Mayall 4m. A thorough scientific analysis of these and other survey

objects is under way and results are being prepared for publication elsewhere. Table III summarizes the observing parameters and conditions. Bad frames, i.e. due to low power because of variable obscuration or to poor guiding and tracking such that part of the specklegram was cut off by the edge of the field, were edited from both data sets. The observing conditions for the first binary were the worst with partially cloudy conditions and significantly poorer seeing. The seeing measurements were obtained after removing the centroid motion for each specklegram and then integrating. Both data sets were reduced using cross-spectrum and shift-and-add analyses described above.

5.1. SHIFT-AND-ADD IMAGES

Figure 8 shows the "raw" SAA images for these objects and their point source references. As can be seen the first object (top) has a well resolved but faint companion in the SW quadrant. Note the elongated structure, along the NS direction, which may be due to either poor alignment and/or the longer exposure time. As it is visible in both the object and the point source, it suggests that the latter will calibrate for it. The second object (bottom) has a barely resolved bright companion almost due east. The improved SNR for these data allow the first Airy ring to be clearly seen, it is barely detectable for the previous object, and the secondary is clearly seen superimposed on it. These images clearly demonstrate the usefulness of the SAA algorithm for the detection and astrometry of companions. However a more detailed analysis is necessary in order to extract the photometry.

5.2. EXTENDED CROSS-SPECTRUM ANALYSIS

Before discussing the results it is important to illustrate the need for applying multiple shifts for the cross-spectrum analysis. Except for the very brightest objects, e.g. K $\sim$ 1 – 2, it has been found that the multiple cross-spectrum shifts, i.e. $\Delta u, \Delta v > 1$, are necessary. This is nicely demonstrated in figure 9 which shows reconstructed images using relaxed phases after using (a) 1 pair, (b) 3 pairs and (c) 5 pairs of sub-planes for the close binary. Note that in the first case, the phases are somewhat scrambled placing the secondary to the NW whereas for the second case the SE lobe has become more dominant but there is still evidence for a NW lobe. For the final case, the NW lobe is no longer visible and the binary nature of the object is now clearly seen. Note the 2% – 4% noise in the final reconstruction.

5.3. RECONSTRUCTED IMAGES

Figures 10 & 11 show the reconstructed images after applying iterative deconvolution to (a) the cross-spectra and (b) SAA results for the two binary

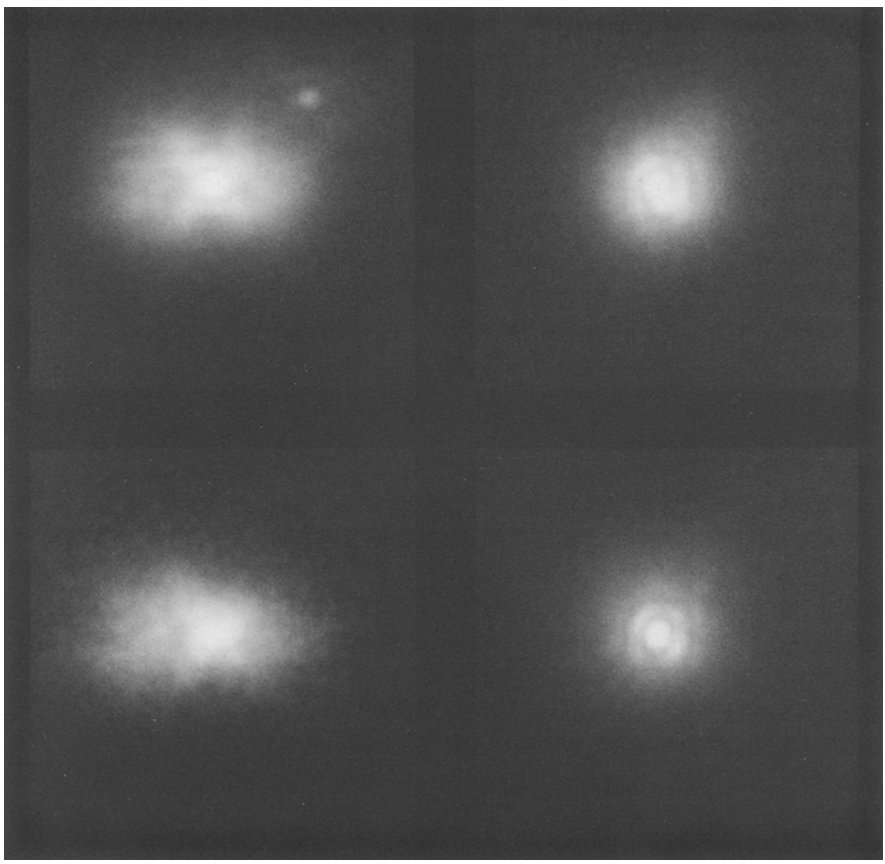

Fig. 8. Raw SAA images for the two observed binaries with point source references on the left and binaries on the right. Note the faint companion to the first binary in the SW quadrant and a brighter companion to the second binary to the E almost at the resolution limit.

stars. Because of the small number of data frames, poor seeing, and longer exposure time as the object is fainter, the effective cut-off frequency for the first binary corresponds to a pupil of $\sim$ 2.3 m giving a resolution, at K, of 0.″200. As can be seen the binary structure is well resolved and both results for the first binary demonstrate a dynamic range of $\sim$ 50:1.

For the second binary the SNR was much better going out to $\sim$ 85% of the cut-off frequency giving a resolution of 0.″140 corresponding to a 3.2 m pupil. The two images show similar southerly systematic structure at $\sim$ 4% level. As it is common to both reductions the implication is that

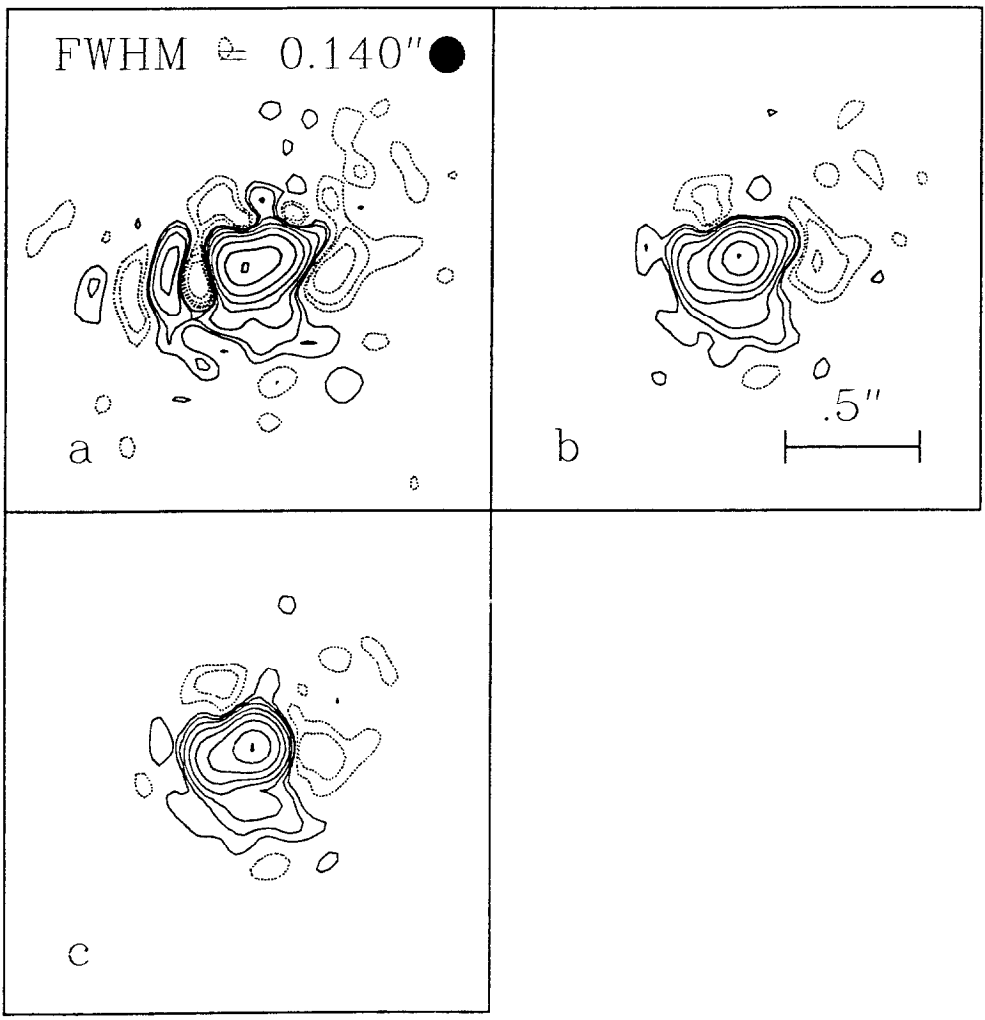

Fig. 9. Reconstructed images for the second observed binary obtained from extended cross-spectrum analysis for (a) 1, (b) 3, & (c) 5 pairs of sub-planes illustrating the necessity of using more than one pair. Note that the same Fourier modulus was used and that the differences are due to the relaxed phases only.

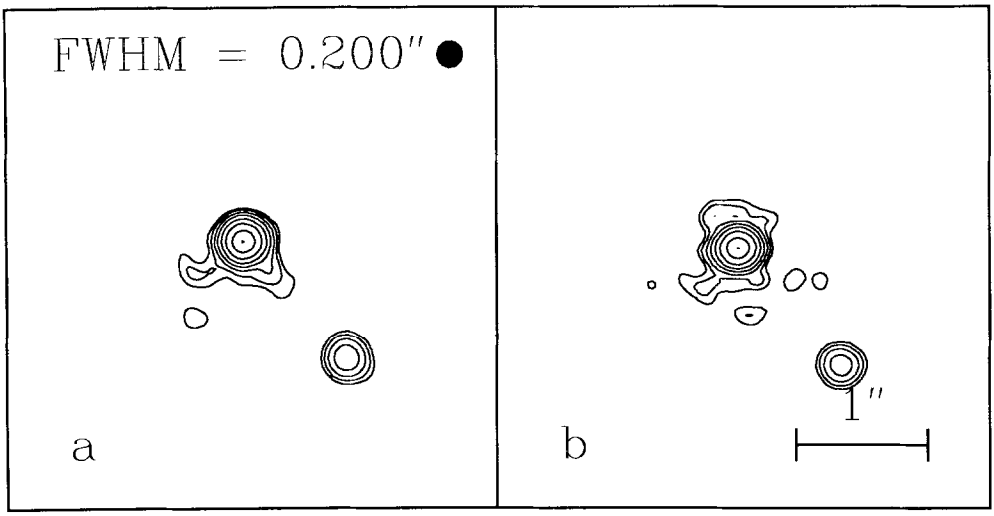

Fig. 10. Reconstructed images of Binary 1 after applying iterative deconvolution with (a) cross-spectrum and (b) SAA analysis. Note that the dynamic range is ~ 50:1.

it is inherent to the object or point source data and not an artifact of the procressing technique. To investigate this further the data were split into subsets and reduced independently. A comparison of the images showed low-level ~ 4% structure which did not occur at the same location indicating that it was seeing noise and not inherent in either data set. This implies that the trustworthy dynamic range of these images is ~ 25–30:1.

As for the simulated data the images and the Fourier moduli were fit with a non-linear least squares algorithm. Table IV compares the binary star parameters obtained for both data sets using the two techniques. For the first object, the wide binary, the two compare very favourably with only a ~ 2% difference in the intensity ratios between the SAA and cross-spectrum reductions. For the closer binary, there is more uncertainty about the position angle with ~ 5° difference between the modulus fit and the image fit and with ~ 4% variation in the intensity ratio. Note that the separation angle is equivalent to the resolution indicating that this companion could not have been detected unambiguously with a smaller aperture. The first minimum in the visibility or Fourier modulus, occurs at ~ 4 cycles/" which corresponds to the resolution of a 1.8 m aperture at the same wavelength. A larger aperture is then needed to detect the upward trend at the higher spatial frequencies above the noise level otherwise the difference between a secondary and a spatially extended object could not be determined. Also note that the SAA image of the close binary shows a similar "ghosting" as

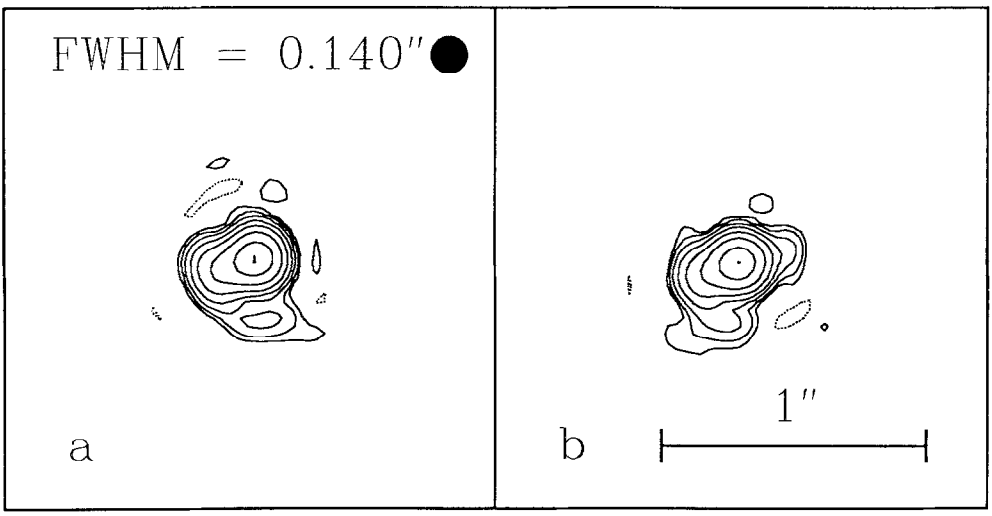

Fig. 11. As for figure 10 but for Binary 2. Note the similar $\sim$ 4% level systematic structure which is common to both reductions and is probably due to seeing calibration errors.

seen for the close binary simulation results. This has the effect of reducing the intensity ratio as derived from the image by $\sim$ 5% which is similar to the simulation.

5.4. ITERATIVE DECONVOLUTION

The ability of the iterative deconvolution procedure to "clean" the Fourier moduli is shown in figures 12 (binary 1) & 13 (binary 2). Both figures show the Fourier modulus before (left) and after (right) iterative deconvolution for SAA analysis (top) and cross-spectrum analysis (bottom). The improved SNR of the latter is clearly evident for both objects. Note the effective cut-off frequency due to SNR shows a greater EW extent of the signal for the first binary. This is consistent with the SAA images shown in figure 9 where the peak (i.e. mean brightest speckle) is more extended in the NS direction. For the second binary the signal support is much more circular as expected from the raw SAA images. The "cleaned" moduli are shown truncated at the cut-off frequency of the Airy beam used to filter them before applying the non-negativity constraints in the image domain. Thus there is no attempt at super-resolution. For both objects, the iterative deconvolution yields very similar results for the two processing schemes which is also suggested by the least-squares fitting. Besides the inherent smoothing of the fringes as expected from the simulations, the two techniques also show self-consistent

TABLE IV
Binary star parameters from real data

Object	Technique		Intensity Ratio	Separation (″)	Position Angle (°)
Binary 1	XS	Image	0.14	1.16	222
		Modulus	0.14	1.16	222
	SAA	Image	0.12	1.16	222
		Modulus	0.12	1.16	222
Binary 2	XS	Image	0.38	0.14	109
		Modulus	0.36	0.14	105
	SAA	Image	0.32	0.14	110
		Modulus	0.35	0.14	107

low contrast variation within each data set implying that these features are inherent in the data and are not artifacts of either processing scheme. As in the simulation case the Fourier phases are also smoothed substantially.

6. Summary and Discussion

This article summarizes the reduction procedures currently in use at KPNO and SO to reduce two-dimensional infrared speckle interferometry data. Binary stars represent the majority of objects observed with this technique. As they are the simplest type of resolved object, it is important that the reduction procedures can successfully image them. Implementations of cross-spectrum and shift-and-add analysis to both simulated and real data show that both can sucessfully image the binary stars to within a few percent accuracy. Model fitting of the separation vectors and intensity ratios to both Fourier amplitudes and images confirm this.

The iterative deconvolution procedure to "clean" the images was successfully applied to both the SAA and cross-spectrum reductions by using *a priori* object constraints such as non-negativity. This resulted in a neighbourhood averaging in the Fourier domain without appearing to affect the photometry of the reconstruction as evidenced by the Fourier moduli shown in figures 12 and 13. This gives it an advantage over some applications of the far more complicated maximum entropy algorithm.

Although cross-spectrum analysis appeared to fare better, SAA analysis represents what can be accomplished with an initial investigation of the data before attempting the full Fourier analysis. As such it represents a simple and effective tool for extracting not only the astrometry but also the photometry of binary stars. The modulus of the SAA image obtained from the point source calibration compares very favourably with that obtained from

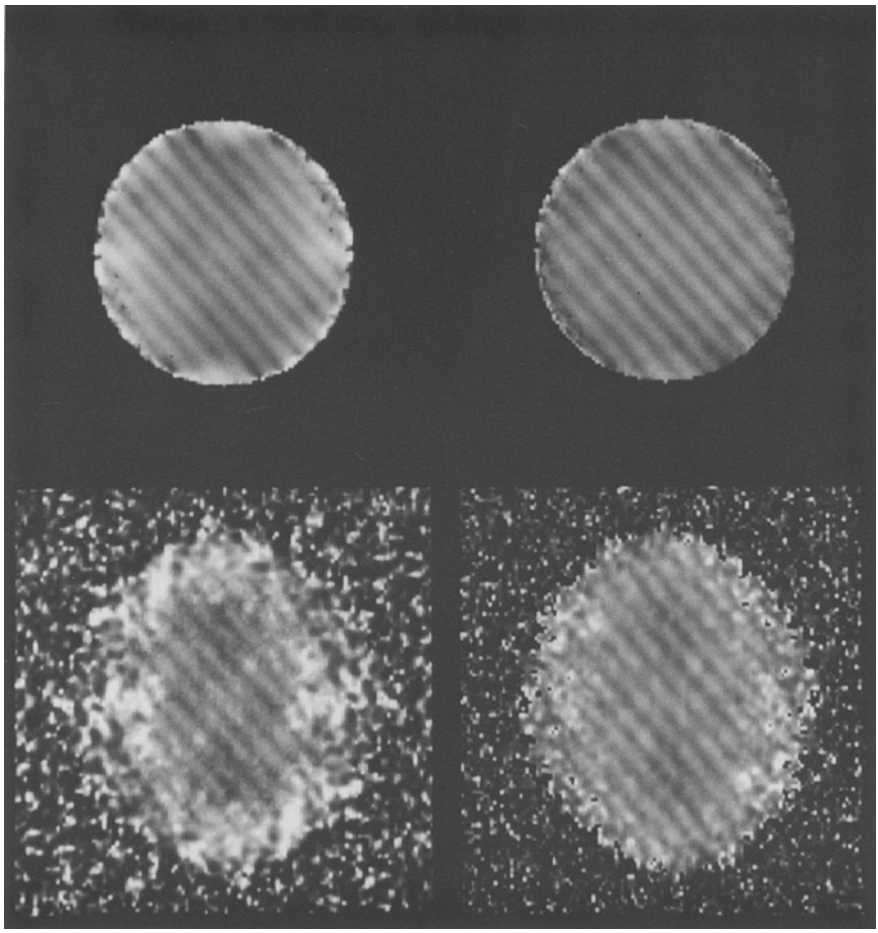

Fig. 12. Fourier moduli for Binary 1 using SAA (top) and cross-spectrum analysis (bottom) before (left) and after (right) iterative deconvolution. Note the multiple fringes due to the wide binary and also note the systematic low contrast features common to both cleaned moduli indicate it is inherent in the data and not the reduction processes.

conventional power spectrum analysis especially after applying the iterative deconvolution. The moduli in figures 12 and 13 nicely illustrate this and even show similar background structure indicating that it is inherent in the data and not an artifact of the processing. However, the presence of ghosts due to the random additive noise favouring the secondary as compared to the primary affects the phases and therefore the reconstructed images. Even so, the reconstruction of the close real binary was far more successful with SAA than by using only one sub-plane of the cross-spectrum to obtain the phases as illustrated in figures 11 and 9 respectively. Bagnuolo (1982) predicts that

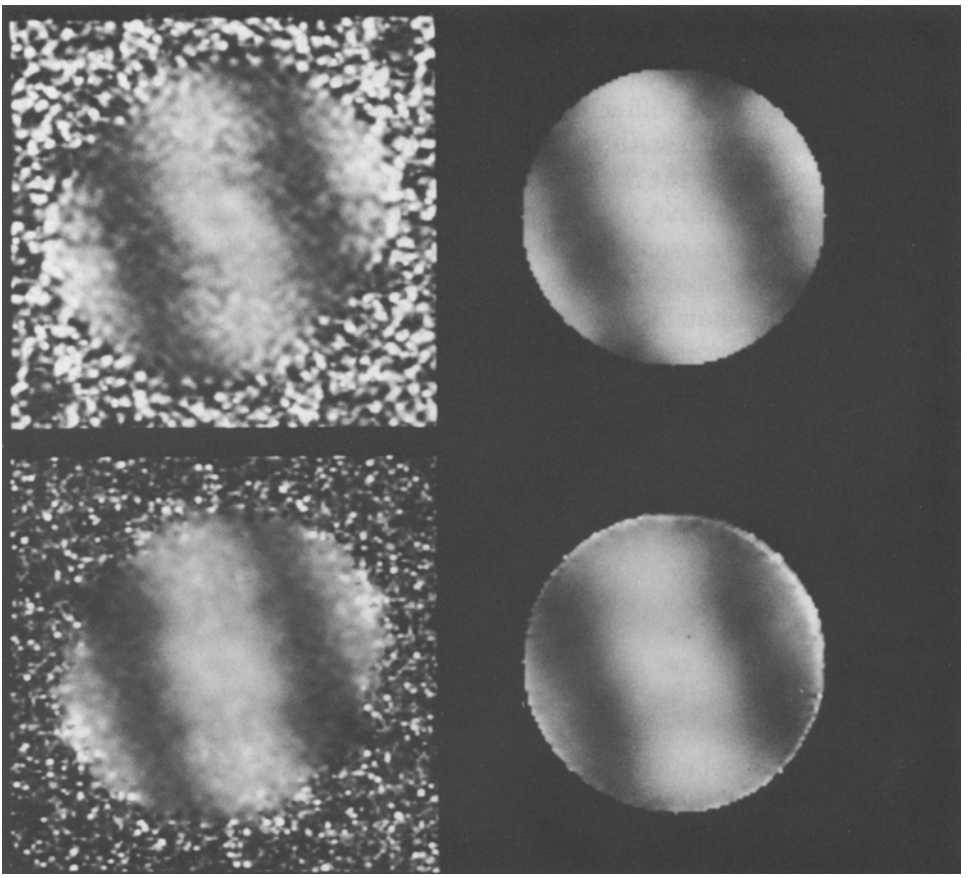

Fig. 13. As for figure 12 but for Binary 2.

the smaller the intensity ratio between the secondary and the primary, the smaller the ratio of the ghost intensity to the secondary. However, this does not appear to be true for the results presented here. Both real and simulated close binaries have larger ghost–secondary ratios than predicted. This can be explained as being due to greater uncertainty in locating the brightest speckle because of the noise and the closeness of the two components which would favour a peak in the direction to the secondary. A similar peak uncertainty occurs for an extended object but with no preferential direction. If the binary had a greater separation the ratio would be expected to be much lower.

A fundamental limitation with SAA analysis is the need to have a point source, or point-like source within the field producing the brightest speckle. For low-contrast extended objects, locating the maximum of the brightest speckle becomes more difficult in that it is now spread over many pixels. In noisy conditions, even with Nyquist sampling, a one pixel error or greater can cause the peak of the SAA image to become even more blurred. A recent improvement to the SAA algorithm which cross-correlates the running SAA estimate with the current frame (Gingras & Aruga, 1990) would improve on this and also the so called "ghosts" or spurious secondary images caused by measuring noise ambiguities. However, such an improvement then makes the SAA process more computationally complex removing its current, but limited, advantage over the full cross-spectrum analysis.

The sucessful SAA deconvolutions presented here illustrate that wider field imaging utilising SAA on a bright point source in the field would also be sucessful. Initial experiments with $\sim 10''$ field of the BN source (Dougados *et al.*, 1991b) have successfully detected previously unknown faint structure. How large a field this can be applied to depends upon the isoplanicity of the proceedure, i.e. to what spatial extent the motion of the bright speckle in one speckle cloud correlates with that in another speckle cloud measured simultaneously. Within this isoplanatic patch, nearby extended objects could then be imaged using the point source SAA image as point spread function. The size of this patch still needs to be investigated as well as the trade-off in reduction of isoplanicity for simultaneity of observations which removes the problem of variable seeing between object and point source.

The dynamic range of the results presented here is $\sim$ 50:1. Can this be improved upon? Experiments with the SO camera have shown that careful calibration is essential, not only for flatfielding but in the choice of the point source references. The former is an instrumental effect and is therefore under some control. However, as more sensitive larger format arrays become available, flatfielding will become more important. Seeing differences between the object and the point source reference limit the amplitude calibration. The use of nearby point sources and frequent switching between them and the objects is very important to minimise the seeing effects.

Increasing the exposure time has been found to be useful for fainter sources such as the wide binary. The moduli in figure 12 indicate that the diffraction-limit is still reached and one second exposure times of point sources show power out to the diffraction-limit, albeit reduced from shorter t_{exp}.

Acknowledgements

The author would like to thank Drs. E.K. Hege, O. von der Lühe, G. Ayers and D.W. McCarthy for valuable discussions concerning the application of the reduction algorithms and also Drs. H. Zinnecker, A. Duquennoy and their colleagues for permission to present some of these results.

References

Ayers, G.R., *Opt. Lett.*, **14** 1165-1167, 1989.
Bagnuolo, W.G., *Mon. Not. R. Astr. Soc.*, **200**, 1113-1122, 1972.
Bates, R.H.T., & Cady, F.M., *Opt. Commun.*, **32**, 356–369, 1980.
Bates, R.H.T, *Physics Reports*, **90**, 203–297, 1982.
Bates, R.H.T. & Davey, B.L.K., *Proc. SPIE*, **828**, 87–91, 1987.
Beckers, J.M., Christou, J.C., Probst, R.G., Ridgway, S.T., & von der Lühe, O., *Proc. NOAO/ESO conference on "High-Resolution Imaging by Interferometry"*, ed. F. Merkle, 393–400, 1988.
Bevington, P.E., "Data Reduction and Error Analysis for the Physical Sciences", McGraw–Hill, 56–65, 1969.
Christou, J.C., Freeman, J.D., Roddier, F. McCarthy, D.W., Cobb, M.L., & Shaklan, S.B., *Proc. SPIE*, **828**, 32–39, 1987a.
Christou, J.C., McCarthy, D.W. & Cobb, M.L., *Astron. J.*, **94**, 416–522, 1987b.
Christou, J.C., *Proc. NOAO/ESO conference on "High-Resolution Imaging by Interferometry"*, ed. F. Merkle, 97–112, 1988.
Christou, J.C., Beckers, J.M., Freeman, J.D., Ridgway, S.T., & Probst, R.G., *Proc. SPIE*, **976**, 193–202, 1988.
Christou, J.C., *Proc. SPIE*, **1237**, 424–435, 1990.
Christou, S.T., Ridgway, S.T., Haniff, C.A., Buscher, D.F., & McCarthy, D.W., *Proc. NOAO/KPNO Conf. on Astrophysics with Infrared Arrays*, ed. R. Elston, Astr. Soc. Pac., 133–138, 1991.
Christou, J.C., *Publ. Astron. Soc. Pac.*, submitted, 1991.
Dainty, J.C., & Fienup, J.R., in *Image Recovery: Theory and Applications*, ed. H. Stark, Academic, 231–275, 1987.
Dougados, C., Léna, P., Ridgway, S.T., Christou, J.C., & Probst, R.G., *Proc. NOAO/KPNO Conf. on Astrophysics with Infrared Arrays*, ed. R. Elston, Astr. Soc. Pac., 152–154, 1991a.
Dougados, C., Léna, P., Ridgway, S.T., Christou, J.C., & Probst, R.G., *Proc. NOAO/KPNO Conf. on Astrophysics with Infrared Arrays*, ed. R. Elston, Astr. Soc. Pac., 258–260, 1991b.
Ebstein, S.M., Ph.D. Thesis, Harvard Univ., 1987.
Gingras, D.J. & Aruga, T., *Opt. Lett.*, **15**, 1380–1382, 1990.
Haas, M., *Astron. Astrophys.*, **236**, 531–543, 1990.
Haniff, C.A., Buscher, D.F., Christou, J.C., & Ridgway, S.T., *Proc. SPIE*, **1237**, 259–271, 1990.
Hege, E.K., *in Diffraction-limited Imaging with Very Large Telescopes*, ed. D.M. Alloin & J.-M. Mariotti, Kluwer, 141–155, 1989.
Knox, K.T., *J. Opt. Soc. Am.*, **66**, 1236, 1976.
Labeyrie, A., *Astron. & Astrophys.*, **6**, 85–87, 1970.
McCarthy, D.W., McLeod, B.A., & Barlow, D., *Proc. SPIE*, **1237**, 496–507, 1990.
McCarthy, D.W., Henry, T.J., McLeod, B.A., & Christou, J.C., *Astron. J.*, **101**, 214–219, 1991a.
McCarthy, D.W., McLeod, B.A., Freeman, J.D., Wizinowich, P.L. & Christou, J.C., *Astrophys. J.*, submitted, 1991b.

Nisenson, P., *in Diffraction-limited Imaging with Very Large Telescopes*, ed. D.M. Alloin & J.-M. Mariotti, Kluwer, 157–169, 1989.
Perrier, C., & Mariotti, J-M., *Astrophys. J. (Letters)*, **312**, L27, 1987.
Perrier, C., *in Diffraction-limited Imaging with Very Large Telescopes*, ed. D.M. Alloin & J.-M. Mariotti, Kluwer, 99–111, 1989.
Skilling. J. & Bryan, R.K., *Mon. Not. R. Astron. Soc.*, **211**, 111, 1984.
Southwell, W.H., J. Opt. Soc. Am., **70**, 998-1006, 1980.
von der Lühe, O., *Proc. ESO/NOAO Joint Workshop on "High Angular Resolution From The Ground Using by Interferometric Techniques"*, ed. J. Goad, 37–41, 1987.
Zinnecker, H., Christou, J.C., Ridgway, S.T., & Probst, R.G., *Proc. NOAO/KPNO Conf. on Astrophysics with Infrared Arrays*, ed. R. Elston, Astr. Soc. Pac., 270-272, 1991.